Engineering Antioxidant and Oxygen-Releasing Lignin Composites to Accelerate Wound Healing

Swathi Balaji[1]*, Walker D. Short[1], Benjamin W. Padon[1], Tanuj J. Prajapati[1], Fayiz Farouk[1], Aditya Kaul[1], Jorge A. Belgodere[2], Sarah E. Jimenez[2], Naresh T. Deoli[3], Anna C. Guidry[2], Justin C. Green[2], Dongwan Son[4], Sonya Keswani[1], Olivia S. Jung[2], Carlos E. Astete[2, 5], Myungwoong Kim[4], Jangwook P. Jung[2]*

[1]Division of Pediatric Surgery, Department of Surgery, Texas Children's Hospital and Baylor College of Medicine, Houston, TX
[2]Department of Biological Engineering, Louisiana State University, Baton Rouge, LA
[3]Louisiana Accelerator Center, University of Louisiana at Lafayette, Lafayette, LA
[4]Department of Chemistry and Chemical Engineering, Inha University, Incheon, Republic of Korea
[5]Louisiana State University Ag Center, Baton Rouge, LA

*Corresponding authors:
Jangwook P. Jung, Ph.D.
Louisiana State University
Department of Biological Engineering
167 E.B. Doran Hall
Baton Rouge, LA 70803
Phone: (225) 578-2919
Fax: (225) 578-3492
E-mail: jjung1@lsu.edu

Swathi Balaji, Ph.D.
Texas Children's Hospital and Baylor College of Medicine
Feigin Center, C.450.05
1102 Bates Ave.
Houston, TX 77030
Phone: (832) 824-0461
Fax: (832) 825-3141
Email: balaji@bcm.edu

ABSTRACT

The application of engineered biomaterials for wound healing has been pursued since the beginning of tissue engineering. Here, we attempt to apply functionalized lignin to confer antioxidation to wound extracellular microenvironments and to deliver oxygen via calcium peroxide for enhanced vascularization and healing responses without eliciting inflammatory responses. We demonstrated *in vitro* that thiolated lignosulfonate in alkene-incorporated gelatin effectively promoted the expression of angiogenesis and extracellular matrix production genes and attenuated the expression of oxidative stress genes of human dermal fibroblasts. Elemental analysis of oxygen releasing nanoparticles showed the positive incorporation of calcium peroxide. Lignin composites including nanoparticles of sodium lignosulfonate and calcium peroxide released around 0.05% oxygen per day at least for 7 days. By modulating the concentration the alkene-incorporated gelatin, we were able to maintain the injectability of lignin composite precursors and the stiffness of lignin composites after photo-crosslinking. *In situ* formation of lignin composites with oxygen generation nanoparticles enhanced the formation of blood vessels and promoted infiltration of α-smooth muscle actin^{+} fibroblasts into the wounds over 7 days. At 30 days after surgery, the lignin composite with oxygen generating nanoparticles remodeled the collagen architecture resembling to the reticular pattern of normal collagen with minimal scar formation. Thus, our study shows the potential of functionalized lignosulfonate for wound healing applications requiring balanced antioxidation and controlled release of oxygen for enhanced vascularization and maturation of collagens.

INTRODUCTION

Wound healing is a critical process which progresses through tightly regulated phases and ultimately leads to repopulation of the wound with cells and extracellular matrix (ECM) to repair the injured site. In response to injury, several amphibians can heal regeneratively, including entire limb restoration, spontaneously throughout their lifetime[1]. While such regenerative healing in mammals is limited to the mid-gestation fetus, late gestation and postnatal mammals fail to regenerate skin or any of their injured organs. They heal with scar tissue formation with less integrity and limited functional capacity as compared to uninjured tissues. This inherently deficient process is further exacerbated in chronic and non-healing wounds. there is a significant clinical need for wound treatments that promote successful and “regenerative” healing.

A key aspect of the wound healing process involves the production of granulation tissue, a densely vascularized provisional tissue composed of fibroblasts (FBs), vascular endothelial cells (ECs), inflammatory cells and cell-derived ECM. Poor vascularization of the granulation tissue is often associated with impaired healing. Previous studies of vascular morphogenesis have revealed an essential role for FBs in the formation and maintenance of vascular networks by secreting soluble factors and ECM components[2-4]. The cytokine/chemokine signaling by FB also prime the local microenvironment, recruit an array of immune cells, including leucocytes, monocytes and macrophages and modulate their polarization and function. Crosstalk between fibroblasts (FBs), endothelial cells (ECs) and macrophages (Mφ) is emerging as a key regulator that promotes either resolution or aberrant remodeling that leads to excessive inflammation and scar production in impaired and chronic wounds[5-9]. Recent evidence further links excessive production of ROS (reactive oxygen species) and/or impaired detoxification of ROS to the pathogenesis of impaired wound healing[10-12]. Excess ROS accumulation disrupts cellular homeostasis and causes non-specific damage to critical cellular components and function, leading to impairment such as abhorrent FB collagen synthesis[13] and cell apoptosis, EC and smooth muscle cell dysfunction and compromised tissue perfusion, and increased proinflammatory cytokine secretion by macrophages[14]. Excess ROS is scavenged by enzymes such as superoxide dismutase and antioxidants that regulate the redox environment in healing skin wounds.

In recent years, antioxidants have drawn much attention as potential therapeutic interventions due to their ability to fight oxidative stress[15-21]. The main function of antioxidants is to

scavenge or neutralize free radical formation and to inhibit the deleterious downstream effects of ROS. However, most antioxidants, taken orally, have limited absorption profile, which leads to low bioavailability and insufficient concentrations at the target site[22,23]. To overcome this issue, research has been focused on developing tissue engineering strategies to provide locoregional delivery of antioxidants. Strategies including antioxidant nanoparticles made of inorganic materials such as mesoporous silica, cerium oxide, and fullerene, have been evaluated in *in vitro* assays and in animal models to determine their ability to scavenge free radicals while decreasing ROS concentrations to protect cells against oxidative stress[24-27]. Hydrogels that release ROS scavengers have been developed to promote cell function as a method to mitigate the foreign body response[28]. However, currently utilized biomaterials, especially natural biomaterials, employ relatively complex chemistry and lack mechanical tunability[29].

For successful application of engineered biomaterials for wound healing, it is imperative to overcome the limitation of oxygen diffusion via exogenous oxygenation such as using perfusion bioreactors. In a small scale oxygenation, many solid inorganic peroxides have been used to support cell growth, survival, tissue regeneration, and bioremediation[30]. Calcium peroxide (CaO_2) possesses many distinctive properties in comparison with other peroxides when it is used as disinfectant and oxygen generator, including better thermal stability, environmental harmless end products, extended release period of hydrogen peroxide and reasonable cost[31,32]. The amount of oxygen released by inorganic solid peroxides depends on their solubility coefficients. The equilibrium coefficients of calcium and magnesium peroxide are 9.8×10^{-11} and 1.8×10^{-11}, respectively[33]. Calcium and magnesium peroxide have low solubility coefficients, 1.65 mg/mL at 20°C and 0.86 mg/mL at 18°C, respectively[33]. Based on these values, calcium peroxide has a higher oxygen-generation potential than magnesium peroxide[33,34].

To apply antioxidation and locoregional oxygenation, we developed injectable lignin composites with the following components: 1) thiolated lignosulfonate (TLS) scavenges ROS from wounds[35], 2) methacrylated gelatin (GelMA) modulates the mechanical properties of lignin composites to support injectability, and 3) sodium lignosulfonate (SLS)[36] encapsulate calcium peroxide in NPs of SLS while scavenging radicals from CaO_2[36,37] while protecting CaO_2 from aqueous environment. First, we assessed the integration of CaO_2 to NPs of SLS and the release of O_2 from lignin composites including all three components. Then, swelling/degradation profiles and mechanical properties and of lignin composites were assessed. Lastly, we applied lignin composites in the wounds of wildtype mice and assessed granulation tissue, neovascularization and wound healing process, inflammatory responses and scaring.

MATERIALS AND METHODS

Synthesis of NPs of CPO or CPOc

The coupling of lignin to PLGA (poly(lactic-*co*-glycolic) acid) was performed by acylation reaction for SLS[36] in a mass ratio of 2 to 1. The final precipitate was collected and dried for 2 days under high vacuum. Then, SLS-*graft*-PLGA was dissolved in ethyl acetate (organic phase) and calcium peroxide (Cat# 466271, Sigma-Aldrich, St. Louis, MO, USA) and dissolved under stirring at room temperature. The organic phase was added to the aqueous phase (low resistivity water) under stirring. The suspension was homogenized with a microfluidizer (Microfluidics Corp., Westwood, MA, USA) at 30 kpsi at 4°C. Next, the organic solvent was evaporated with a rotary evaporator R-300 (Buchi Corp, New Castle, DE, USA). Finally, trehalose was added (1:1 mass ratio) as a cryoprotectant for the lyophilization of SLS:PLGA NPs and stored at -20°C for further characterization and experiments. To prevent confusion, only NPs of CPO (accordingly CPOc) is abbreviated as CPO and raw calcium peroxide (CaO_2) is not abbreviated in the manuscript.

Dynamic light scattering (DLS) of NPs

Size, polydispersity and ζ-potential of NPs of CPO and TLS (0.2-0.4 mg/mL) were measured by dynamic light scattering (DLS) using Malvern Zetasizer ZS (Malvern Panalytical, Westborough, MA, USA). NP suspensions were filtered through 0.45 μm filter. To prevent the formation of disulfide bonds, TLS sample was prepared in 250 mM Tris(2-carboxyethyl)phosphine hydrochloride (TCEP HCl, Cat# H51864, Alfa Aesar, Haverhill, MA, USA) in PBS.

Elemental analysis of NPs of TLS, CPO and CPOc

We utilized the nuclear microscopy setup at the Louisiana Accelerator Center to probe the calcium concentrations in our samples using particle-induced x-ray emission (PIXE) spectrometry[38]. The samples were placed in a low-pressure environment ($\leq 1\times10^{-6}$ mbar) on electrically conductive non-porous carbon tape attached to the sample holder. A focused (10 μm × 10 μm) 2 MeV proton beam, with a beam current in the range of 10−20 pA, raster scanned the sample region (1 mm × 1 mm) for about 1 h. A silicon drift detector was placed at 135° in front of the sample to detect the characteristic x-rays excited by energetic protons. Analysis of the spectra was performed with the GeoPIXE™ software (v7.3)[39]. The elemental maps and the derived concentrations were generated by the dynamic analysis method using average matrix composition from the whole scanned area.

Formation of lignin composites

TLS was synthesized with the previously published protocol[35]. GelMA was synthesized by the coupling reaction of gelatin with methacrylic acid (see supplementary information for details). We confirmed the alkene incorporation to gelatin with ^{1}H nuclear magnetic resonance (NMR, **Figure S1**). Lignin composites were formed by weighing out GelMA, lithium phenyl-2,4,6-trimethylbenzoylphosphinate (LAP, Allevi, Philadelphia, PA, USA) and NPs of TLS, CPO or CPOc (SLS:PLGA NP without CPO). A TLS lignin composite is GelMA crosslinked with NPs of TLS. A CPO lignin composite is a TLS lignin composite including NPs of CPO. A CPOc lignin composite (CPOc) is a TLS lignin composite including NPs of CPOc. For the fibrosis array, the concentrations of GelMA and LAP were fixed at 80 and 5 mg/mL, respectively. Any concentrations of TLS higher than 7 mg/mL interfered photo-crosslinking of lignin composites, leading to the reduction of elasticity of lignin composites with partially crosslinked lignin composites. All other experiments, the concentrations of GelMA, LAP and TLS were fixed at 50, 5 and 3 mg/mL, respectively and the concentrations of CPO or CPOc were varied at either 4 or 40 mg/mL. The precursor of lignin composites was prepared by mixing GelMA in PBS at 37°C and the rest of LAP, TLS and NPs of CPO or CPOc in PBS. Each precursor was pipetted into a custom polydimethylsiloxane (PDMS) mold (8 mm diameter and 1 mm height, 50 μL) to form lignin composites. Samples were crosslinked using an UV floodlamp (Intelli-Ray 400, Uvitron international, West Springfield, MA, USA) for 120 s at 10 mW/cm^2.

Quantification of O_2 release from lignin composites

The released O_2 was optically measured by a planar O_2 sensor spot (SP-PSt3-SA23-D5-OIW-US, PreSens, Regensburg, Germany) placed at the bottom of a 96-well plate. Lignin composites (5 mm diameter and 1 mm height, 20 μL) were placed on top of the planar O_2 sensor spot and submerged in serum-free medium (37°C/5% CO_2). To prevent evaporation, each well was covered with parafilm and the entire plate was wrapped with parafilm. A polymer optical fiber (POF-L2.5-2SMA, PreSens, Regensburg, Germany) optically sensed the concentration of O_2 through the bottom of a well and sent signals to an O_2 sensor (OXY-1 SMA, PreSens, Regensburg, Germany)[40] for measurement.

Swelling ratio and *in vitro* degradation of lignin composites

Swelling ratios of lignin composites were determined by the following equation: $[W_s-W_d]/W_d$, where W_s and W_d represent the weight after swelling in PBS for 24 h and the weight after lyophilization, respectively. *In vitro* degradation of lignin composites was determined by submerging lignin composites in the solution of collagenase type II (0.5 U/mL, cat# CLS-2, Worthington Biochemical) with 1 mM $CaCl_2$ in serum-free culture medium (see details in Cultures of human dermal fibroblasts), along with a control group without including the collagenase. Lignin composites were collected at 0, 2, 6 and 24 h and lyophilized to determine the fraction of remaining composites.

Oscillating rheometry of lignin composites

Using a TA Discovery HR-2 rheometer and the previously published methods[35], viscosity of the precursors of lignin composites were measured in a flow ramp setting (shear rate from 1 to 2000 (1/s)) and with a 25 mm parallel plate. Using an 8 mm parallel plate, storage (G′) and loss (G″) moduli of lignin composites were determined by frequency sweeping from 0.62 to 19.9 (rad/s) at 2% strain. Since storage moduli are altered by axial stress applied during measurement, we evaluated the slope of axial stress vs compression, similar to evaluating Young's modulus from the slope of a stress-strain curve[41]. Axial stresses at 0, 10 and 20% of compression were determined, while composite samples were subject to 2% strain and 6.28 rad/s frequency.

Cultures of high and low scar normal human dermal fibroblasts

Skin tissue was collected from abdominoplasty patients who provided written informed consent as part of a protocol approved by the Institutional Review Board of Texas at Baylor College of Medicine in accordance with the Declaration of Helsinki. A biobank of scar and matched normal uninjured skin tissue was obtained from abdominoplasty patients controlled for sex, age, ethnicity, surgery type, indication, wound site, and comorbidities. These skin tissues were grouped into 'low scarring' and 'high scarring' phenotypes based on the evaluation of their existing c-section scars using Vancouver Scar Scale (VSS). Skin obtained from patients with 1-3 score on VSS were categorized as 'low scarring' phenotype (N) and patients with 6-9 score were grouped into 'high scarring' phenotype (S). For each group, n=3 skin tissues were pooled. Fibroblasts (FBs) were isolated from scar and matched normal skin cohorts and were called 'low scarring' (LS) and 'high scarring' (HS) normal fibroblasts based on their VSS phenotype and patient demographics. Only LS-normal and HS-normal human dermal FBs (hdFBs) were used for cell studies, and they are denoted HS and LS for the rest of the studies. Both LS and HS hdFBs were maintained in DMEM (Cat# 10567-014-500mL, Thermo Fisher Scientific, Waltham, MA, USA) supplemented with 10% fetal bovine serum (FBS, Cat# 35-015-CV, Corning, Corning, NY, USA), Penicillin/Streptomycin (P/S, Cat# 15140-122, Thermo Fisher Scientific, Waltham, MA, USA), and antibiotic/antimycotic (anti/anti, Cat# 15240-062, Thermo Fisher Scientific, Waltham, MA, USA). Only passages 8-10 were used for studies and cells were harvested at 80-90% confluency by applying TrypLE Express (Cat# 12604-021, Thermo Fisher Scientific, Waltham, MA, USA) and pelleted at 350 g for 5 min. Supernatant was removed and hdFBs were gently resuspended in cell culture media and counted. Media was changed every other day.

PCR array

To determine the effect of lignin composite on their expression of fibrotic phenotype of hdFBs, LS and HS hdFBs were seeded onto composites at 50,000 cells/cm^2 and maintained for 24 h in a CO_2 incubator (5% CO_2/37°C). At specified time points, cell-seeded composites were removed and incubated with TrypLE Express to extract RNA by following the procedure from the PureLink RNA kit (Cat# 12183018A, Thermo Fisher Scientific, Waltham, MA, USA). Extracted RNA was evaluated for quantity and purity using a Take3 Micro-Volume plate and Cytation3 spectrophotometer (Biotek, Winooski, VT, USA). cDNA was reverse-transcribed using High-Capacity RNA-to-cDNA kit (Cat# 4387406, Thermo Fisher Scientific, Waltham, MA, USA)

following the protocol from the manufacturer. We also used the RT2 Profiler PCR Array human fibrosis kit (Cat# PAHS-120-ZE-4, Qiagen, Hilden, Germany) to detect the expression of 84 fibrosis-related genes. cDNA (400 ng) made with RT2 first strand kit (Cat# 330404, Qiagen, Hilden, Germany) were used with RT2 SYBR Green qPCR Mastermix (Cat# 330501, Qiagen, Hilden, Germany) to run qRT-PCR on Bio-Rad CFX 384 real-time system. Data were analyzed by Qiagen RT2 Profiler PCR array data analysis software. GAPDH was used as a housekeeping gene, and ΔΔCT values for the genes were analyzed. Principal component analysis (PCA) and hierarchical clustering (HC) were performed and visualized with an open source machine learning software (Orange)[42].

Animal model of wound healing

Wound healing studies were carried out in wildtype (WT) C57BL/6N mice (8- to 10-week-old, female and male). Mice were maintained under pathogen-free conditions with access to food and water ad libitum in the Texas Children's Hospital Feigin Center animal facility. Protocols for animal use were approved by the Institutional Animal Care and Use Committee at Baylor College of Medicine. At the time of wounding, mice were anesthetized using isoflurane, the backs were shaved, and prepped for surgery with three times alternating betadine and 70% isopropyl alcohol scrubbing. Two 6 mm diameter full thickness wounds were made using a 6 mm dermal punch biopsy, excising tissue through the panniculus carnosus (PC) muscle. Immediate skin contraction was controlled through application of a silicone stent with inner diameter of 8mm and outer diameter of 16mm, secured concentric to wound using skin adhesive and 6 simple interrupted 6-0 Proline© sutures (Ethicon, Raritan, NJ). Wounds were maintained in a moist wound environment using a semi-occlusive sterile adhesive dressing (Tegaderm, 3M, St. Paul, MN, USA) and contraction was controlled through application of a silicone stent with inner diameter of 8 mm and outer diameter of 16 mm, placed concentric to wound using skin adhesive and 6 interrupted sutures. Prior to dressing with Tegaderm, each wound received one of four treatments: a standard saline wash (untreated, UNTX), GelMA with TLS (TLS), GelMA-TLS with NPs of CPOc (CPOc) or GelMA-TLS with NPs of CPO (CPO). Crosslinking of the treatments was performed immediately after application to the wound bed using a UV floodlamp (B-100AP High Intensity, Blak-Ray) for an exposure time of 30 s.

Wounds were imaged at 1, 3, and 7 days post operatively (**Figure S2**), and harvested at days 7 and 30. For histology and immunostaining, wounds were bisected in the rostral-caudal plane, fixed overnight in 10% neutral buffered formalin, dehydrated through a series of graded ethanol and xylene, and embedded in paraffin wax. Five-micrometer-thick sections from the paraffin-embedded wounds were collected using a RM 2155 microtome (Leica, Heidelberg, Germany) and used in staining.

Morphometric quantification

At day 7, epithelial gap and granulation tissue areas were measured from Hematoxylin and Eosin (Cat#3801571 and Cat#3801615, respectively; Leica, Heidelberg, Germany) stained sections using morphometric image analysis (LASX, Leica, Heidelberg, Germany). Staining was carried out on 5 μm formalin fixed paraffin embedded (FFPE) sections following deparaffinization and rehydration in graded xylene and ethanol as following the manufacturer's recommendations. Epithelial gap was determined using a full, 4× tile scan of the wound bed, and measuring the distance (in mm) between the leading epithelial margins on either side of the wound. Granulation tissue area was determined using a standardized approach of calculating the entire wound area (in mm^2) above the panniculus carnosus and bounded within the wound edges laterally. If parts of the hydrogel remained devoid of infiltrated cells, that area was excluded from the granulation tissue assessment.

Immunostaining

Immunohistochemistry was carried out on serial 5 μm sections from day 7 FFPE tissues, which were deparaffinized and rehydrated to water using graded xylene and ethanol. Primary antibodies used were αSMA (rabbit anti-mouse, Cat# ab5694, Abcam, Cambridge, United Kingdom, 1:500 dilution) to measure myofibroblast infiltration, CD31 (rabbit anti-mouse, Cat# ab28364, Abcam, Cambridge, United Kingdom, 1:100 dilution) to measure endothelial cells and vascular lumen density, CD45 (rabbit anti-mouse, Cat# ab10558, Abcam, Cambridge, United Kingdom, 1:5000 dilution) to determine pan-leukocyte infiltration, CD206 (rabbit anti-mouse, Cat# ab64693, Abcam, Cambridge, United Kingdom, 1:500 dilution) to measure M2 macrophage levels, F4/80 (rat anti-mouse, Cat# MF48000, Thermo Fisher Scientific, Waltham, MA, USA, 1:5000 dilution) to measure pan macrophage infiltration, and Ly6G (rat anti-mouse, Cat# 551459, BD Biosciences, Franklin Lakes, NJ, USA, 1:5000 dilution) to determine infiltration of monocytes, granulocytes, and neutrophils.

Following deparrafinization and rehydration to water, sections were then immersed in target antigen retrieval solution (Cat #K800521-2, Agilent, Santa Clara, CA, USA) and treated following the protocol within the DAKO PT Link Rinse Station (Cat #PT10930, Leica, Heidelberg, Germany). Following antigen retrieval, wound sections were stained using the DAKO autostainer (AS480, Leica, Heidelberg, Germany). First, the sections were buffered in DAKO wash buffer (Cat #K800721-2, Agilent, Santa Clara, CA, USA) before incubating in primary antibody diluted in DAKO antibody diluent (Cat# S080983-2, Agilent, Santa Clara, CA, USA) for 1 h. The primary antibody was then rinsed, and the sections were washed in wash buffer before incubation in the appropriate the secondary antibody system, either HRP-Rabbit (Cat# K400311-2, Agilent, Santa Clara, CA, USA) or HRP-Rat (Cat#D35-110, GBI Labs, Bothell, WA) for 20 min. The secondary antibody was then rinsed off using wash buffer, and the appropriate visualization system was applied – DAKO DAB (Cat# K346811-2, Leica, Heidelberg, Germany) for all but CD206 which utilized AEC (Cat# K400511-2, Leica, Heidelberg, Germany). A hematoxylin (Cat #K800821-2, Agilent, Santa Clara, CA, USA) counterstain was then applied, and sections were dehydrated in graded xylene and ethanol before putting coverslips using a xylene based mounting media (Cat#23-245691, Thermo Fisher Scientific, Waltham, MA, USA) – except for those sections using AEC as the visualization system which required an aqueous mounting media (Cat#108562, Merck KGaA, Darmstadt, Germany).

Staining was quantified using images taken on the Leica DMI8 camera. For all data, the percentage of positive cells were determined by counting the number of positive cells per High Powered Field (HPF, 40× magnification) and dividing by the total number of cells in that HPF as determined by the hematoxylin counterstain. Final values were determined by the average of 4 to 6 HPFs per wound. Total number of vessel lumens were counted per HPF. These percent values or vessel counts were then averaged from 6 images taken across the wound bed to determine the final value.

Scar assessment

Serial 5 μm sections from D30 FFPE tissue were deparaffinized and rehydrated to water using graded xylene and ethanol. Sections were then stained using Gomori's Trichrome (blue) as following the manufacturer's recommendations (Cat# 38016SS2, Leica, Heidelberg, Germany). Collagen content per HPF in the dermis of the scars was measured using established methods with color-thresholding in ImageJ in which color segmentation is used to isolate only blue pixels, representing collagen fibers, thus allowing quantification of the amount of collagen within the selected area[43]. Gross images of the wound at day 30 were also obtained, and a subjective assessment of scarring was performed.

Statistical analysis

For multiple comparisons, one-way ANOVA with Tukey's *post hoc* tests or with Kruskal-Wallis test followed by Dunn's test was performed, where p values <0.05 were considered significant. At least three independent experiments were performed.

RESULTS

3D and TLS composites attenuated the differential expression of genes associated with angiogenesis, ECM production and oxidative stress in LS and HS hdFBs.

Our previous work[35] showed that the antioxidation capacity of TLS attenuated the expression of *COL1A1*, *ACTA2*, *TGFB1*, and *HIF1A* and resulted in the similar extent of expression of the fibrotic markers comparable to proliferative LS hdFB phenotypes. To further confirm that the attenuation of fibrotic phenotypes of hdFBs by TLS composites, we analyzed 84 genes associated with angiogenesis, ECM production and oxidative stress using a PCR array. We hypothesized that exposure of LS and HS hdFBs to engineered TLS composites attenuates these angiogenesis, ECM production and oxidative stress responses of HS to the levels comparable to those of LS. As shown in **Figure 1a**, the expression of fibrotic genes in HS hdFBs on 3D composites was significantly altered to mimic those in LS. In **Figure 1b**, heatmaps showing unsupervised hierarchical clustering (HC) of the expression of angiogenesis, ECM production and oxidative stress genes of LS and HS hdFBs on 3D composites show subsets of genes that are significantly altered in HS to mimic LS. These results and the previous works[35] suggest that optimizing the hdFB microenvironment using lignosulfonate may reduce the effect of inherent differences in hdFBs on their overall fibrotic functions during wound repair.

Elemental analysis confirmed the incorporation of calcium peroxide (CaO_2) in NPs of CPO.

Our effort to apply the antioxidant capability of TLS to wound microenvironments would be synergistic with other pro-regenerative stimuli. We hypothesized that controlled release of oxygen while scavenging ROS by TLS in the wound microenvironments will accelerate wound healing. Thus, we incorporated CaO_2 in SLS NPs[36] and found that the size of SLS NP with CaO_2 (NPs of CPO) is not significantly altered, even when compared to SLS only NP (NPs of CPOc), as shown in **Table 1**. In comparison to SLS, the average diameter of NPs of CPO increased while the PdI of NPs of CPO was significantly smaller than that of NPs of CPOc. SLS is natural biomaterial with potential lot-to-lot variability. However, the synthesis of NP with CaO_2 slightly increased the average diameter and significantly reduced PdI upon the incorporation of CaO_2. In contrast, NPs of CPOc were formed only with ethyl acetate, forming irregular shapes and possible with cavity. In contrast, the average diameter of TLS is significantly smaller than SLS or NPs of CPO or CPOc. After adding TCEP to cleave possible disulfide bonds in TLS, the average diameter of TLS was further reduced. As evidenced in **Table 1**, TLS formed NPs with a broader distribution. The formation of NPs of CPO or CPOc requires stirring at room temperature, while the thiolation of SLS is completed via acid-catalyzed esterification at 80°C. In PBS (pH 7.4), NPs were formed via interparticle disulfide formation with thiols in TLS, but adding TCEP to PBS dissociates NPs of TLS into smaller NPs. This could be an advantage to form lignin composites with homogeneous distribution of TLS in the matrix of GelMA. After the degradation of GelMA, TLS can be cleared by glomerular filtration (5-10 nm).

Table 1. DLS of NPs with and without CPO incorporated.

Nanoparticles	Average dia. ± st. dev. (nm)	PdI_{DLS} (st. dev./mean dia.)^2
SLS	126.6 ± 7.2	0.585 ± 0.017
CPO	140.8 ± 0.5	0.0597 ± 0.0199
CPOc	171.6 ± 1.9	0.204 ± 0.025
TLS	58.01 ± 13.54	0.258 ± 0.056

TLS with TCEP	7.728 ± 0.090	0.442 ± 0.005

dia: diameter
st.dev.: standard deviation

Due to the size (diameter) of NPs, we assessed the incorporation of CaO_2 by particle-induced x-ray emission (PIXE) spectrometry. NPs of CPO and CPOc showed similar composition of elements while the normalized concentration of Ca in NPs of CPO is about 17 times higher than that of NPs of CPOc in the quantitative molecular spectroscopy (**Figure 2**).

Oxygen released from CPO lignin composites was maintained for 7 days.

To measure the release of O_2 from lignin composites, we used a planar O_2 sensor with optical measurement. These planar sensors can measure the concentration of O_2 in liquid or gas. The difference (Δ) of the area under curve (AUC) between lignin composites with NPs of CPO or CPOc was calculated over 1440 min for 7 days. As shown in **Figure 3**, the difference is around 500 ppm (equivalent to 0.05% O_2) per day. As the statistical difference is not detected, the oxygen release is maintained up to day 7. We observed that the swelling of lignin composites over first 24 h contributed to the slightly higher ΔAUC in day 1 than that in day 2 since lignin composites were placed in a well of the 96-well plate with the planar O_2 sensor and serum-free medium was added without achieving equilibrium swelling of lignin composites.

Swelling ratios and rate of degradation were not significantly different with respect to the presence of NPs of CPO or the concentrations of NPs of CPO.

Injected lignin composites are subject to swelling and enzymatic degradation for remodeling. Thus, we assessed the extent of swelling of lignin composites by varying the concentration of incorporated NPs of CPO or CPOc. As shown in **Figure 4a**, the swelling ratios between CPO and CPOc lignin composites were not significantly different at both 4 and 40 mg/mL. With 40 mg/mL of NPs of CPO or CPOc in lignin composites, the swelling ratios were slightly reduced by around 7% (CPO) and 8% (CPOc) without any statistical difference. Apparently, the 10 times higher mass fraction of NPs (regardless CPO or CPOc) in lignin composites contributed to the swelling behavior with marginal difference. To determine the fraction of remaining lignin composites, TLS, CPO (4 and 40 mg/mL) and CPOc (4 and 40 mg/mL) lignin composites were submerged either in collagenase/$CaCl_2$/serum-free medium or $CaCl_2$/serum-free medium. After 24 h, less than 28% of TLS lignin composite (**Figure 4b**), 38% of CPOc lignin composite with NPs of CPOc at 40 mg/mL and 23% of CPOc lignin composite with NPs of CPOc at 4 mg/mL remained (**Figure 4d**) while CPO lignin composites retained around 60% at both 4 and 40 mg/mL (**Figure 4c**). All control groups (SF medium in **Figures 4b-d**) showed minimal (up to 7%) to no changes in the remaining fraction of lignin composites. The concentrations of matrix metalloproteinase (MMP) in inflamed tissue vary from patients to patients. For example, the concentration of MMP-1/18/13 in chronically inflamed dental pulp tissue is 3 ng/mL[44] and MMP-3 in rheumatoid arthritis patients in 350 ng/mL while the health controls have 75 ng/mL[45]. The concentration of collagenase type II was 0.5 U/mL or 430 μg/mL, which is several orders of magnitude higher than the physiological conditions. Native or wounded skin has a plethora of MMPs, their inhibitors and serum proteins, leading to a tighter control of degradation and thus, we expect much slower degradation of lignin composites *in vivo*. Nevertheless, we expect a certain extent of degradation of lignin composites (primarily, GelMA) *in vivo* to transiently protect NPs of CPO from rapid, enzymatic and mechanical degradation while promoting antioxidant activity from lignosulfonate (both NPs of TLS and SLS in NPs of CPO or CPOc).

NPs did not alter the viscosity of the lignin composite precursors while quantity and type of NP modulated the viscoelasticity of lignin composites.

Since lignin composites are subject to needle injection to the wounded areas, we assessed the mechanical properties of lignin composites before and after thiol-ene crosslinking. Viscosity of all five different types of composite precursors was tested and we found no significant difference (**Figure 5a**). Apparently, crosslinked lignin composites exhibited similar viscoelasticity. However, the compressive modulus of elasticity was significantly different upon incorporating NPs of CPO and CPOc. As shown in **Figure 5b** and **Table 2**, TLS lignin composites exhibited the highest modulus of elasticity. Upon incorporating NPs of CPO at 4 or 40 mg/mL, moduli of elasticity were decreased to around 18-19 kPa. While TLS is thiolated SLS to apply thio-ene crosslinking[35], SLS in NPs of CPO or CPOc was not functionalized for crosslinking. Instead, NPs of CPO harness calcium peroxide proximal to PLGA chains[46] while NPs of CPOc were formed without any CaO_2, which may form cavities during lyophilization. This possibly resulted in lowering the elasticity from the compression test during oscillating rheometry. Consequently, higher quantity of NPs of CPOc (40 mg/mL) showed much lowered slope down to 7.27 kPa in comparison to that of CPO or TLS lignin composites. In **Figure 5c**, storage moduli of TLS and CPO lignin composites were similar to each other while those of CPOc lignin composite were significantly different from those of TLS or CPO lignin composites. However, loss tangent (G''/G') of all lignin composites ranged from 0.01 to 0.07 (equivalent to δ (phase lag) ranging from 0.57° to 4°), indicative of well-crosslinked viscoelastic composites (**Figure 5d**). Collectively, the reduction of stiffness by non-crosslinkable NPs of CPO is potentially significant around 40 mg/mL, thus we continued our investigation of oxygen generating capability from lignin composites with NPs of CPO or CPOc at 4 mg/mL and in mouse models of wound healing.

Table 2. Elastic modulus estimated by the slope of axial stress vs compression.

	Slope (Elastic modulus, kPa)	Intercept (kPa)	R^2
TLS	24.9	0.430	0.8960
CPO 4	18.7	0.286	0.9265
CPO 40	18.4	0.329	0.8661
CPOc 4	11.8	0.304	0.9557
CPOc 40	7.27	0.409	0.9290

<u>The area of granulation tissue was modestly increased with CPO lignin composites.</u>

To determine the effect of lignin composites on the progression of wound healing, wounds were harvested at day 7 post-wounding to examine re-epithelialization and granulation tissue formation. After 7 days of wounding, epithelial gap and the area of tissue granulation were assessed. Untreated wounds (UNTX in **Figure 6a**) showed no sign of re-epithelialization as expected. TLS or CPOc lignin composites in **Figure 6a** still showed the separation of GelMA matrix and tissue (insets in **Figure 6a**), while the CPO lignin composite facilitates enhanced integration of the lignin composite into the wounded tissue over 7 days. There was no difference of the rate of the wound closure, as determined by epithelial gap (the distance between the arrows), between UNTX and TLS (5.0±1.4 vs. 5.8±1.2 mm, $p>0.05$), CPOc (5.0±1.4 vs. 4.7±0.8 mm, $p>0.05$), or CPO (5.0±1.4 vs. 4.4±0.7 mm, $p>0.05$) treated mice (**Figure 6b**). We observed a trend of increasing granulation tissue, especially with CPO lignin composite treatment (1.4±0.2 vs. 2.5±1.0 mm^2, $p<0.05$) (**Figure 6c**), which is indicative of healthy healing progress.

<u>Increased vascularity was promoted by the CPO lignin composite over 7 days.</u>

In addition to the increase of granulation tissue, neovascularization is promoted by the CPO lignin composites. Quantification of neovascularization (**Figure 7a**) showed that UNTX has a significantly higher number of $CD31^+$ endothelial cells while the formation of blood vessel was

delayed at day 7 (**Figure 7b**). Staining with the endothelial cell marker (CD31) revealed a greater number of individual $CD31^+$ cells that are not associated with vessels in UNTX wounds (**Figure 7b**) per HPF than TLS- (36.4±19.8 vs. 11.6±6.3%, $p<0.05$), CPOc- (36.4±19.8 vs. 4.2±4.3%, $p<0.01$) or CPO- (36.4±19.8 vs. 15.1±7.7%, $p<0.05$) lignin composite treated wounds. However, there were significantly more vessel lumens (**Figure 7c**) per HPF in the CPO lignin composite- (17.3.2±7.6 vs. 17.3±7.5 vessels/HPF, $p<0.05$) treated wounds as compared to UNTX wounds.

As shown in **Figure 7d**, αSMA^+ cells (brown staining) were limited to the edge of wounds in UNTX and TLS lignin composites. CPO or CPOc lignin composites showed more αSMA^+ cells in the wounds. However, the CPO lignin composite showed a higher numbers of blood vessel formation both at edge and middle of wounds (**Figure 7d**). As several literature showed that the expression of αSMA^+ implicates the development of vasculature[47,48] and expresses in pericytes on capillaries[49]. While the extent of difference at either edge or middle sections was not significantly different (**Figure S3**), the overall trend was an increase with the CPO lignin composites (**Figure 7e**). We observed similar trends in the number of $CD31^+$ cells (**Figure 7b**) and αSMA^+ cells (**Figure 7e**). The expression of αSMA^+ by myofibroblasts (myoFB) is also shown to underlie tissue regeneration in the skin, and the number of αSMA^+ cells decrease as the regeneration process is completed[50]. Thus, neovascularization is promoted, and the wound healing is still in progress by day 7 with the injection of the CPO lignin composite.

<u>Lignin composites did not cause significantly inflammatory responses over 7 days</u>

Following the quantification of granulation tissue and neovascularization, inflammatory responses were assessed by immunohistochemical staining (**Figure 8**). CD45 is expressed by common leukocytes except platelet and red blood cells. Ly6G is expressed by monocytes, granulocytes and neutrophils. F4/80 is used to identify murine tissue macrophages. CD206 is normally expressed on the alternatively activated M2 macrophages (Mφ). As shown in **Figure 8a**, the interface between wounds and lignin composites does not show (indicated by white wedges) significant infiltration of $CD45^+$ cells. Recently, the stiffness of GelMA is known to directs macrophage phenotypes. Soft GelMA matrix (stiffness less than 2 kPa) is more favorable for priming macrophages toward anti-inflammatory (M2) phenotypes with a decreased capacity for spreading in comparison to stiff (over stiffness 10 kPa) GelMA matrix[51]. The lignin composites are in the range of 1-2 kPa of storage modulus (**Figure 5c**), thus likely priming macrophage toward anti-inflammatory (M2) phenotypes. Over 7 days, no significant changes in the expression of the four markers were noticed. There was no significant difference in percentage of $CD45^+$ (pan-leukocyte) cells/HPF across all tested lignin composites when compared to UNTX wounds (UNTX 40.3±5.7 vs. TLS 33.3±1.5 vs. CPOc 38.7±11.7 vs. CPO 34.0±8.2%, $p>0.05$) (**Figure 8b**). A similar trend was observed when looking at monocyte, granulocyte, and neutrophil infiltration as determined through Ly6G staining (**Figure 8c**). There were no significant differences in the percentage $Ly6G^+$ cells/HPF among treatment groups (UNTX 24.0±11.0 vs. TLS 29.1±8.1 vs. CPOc 29.3±6.3 vs. CPO 25.1±10.5, $p>0.05$). In particular, alternatively-activated M2 macrophages are important mediators of successful wound healing[52]. F4/80 and CD206 staining (**Figure 8c-d**) showed that UNTX wounds had no statistically significant differences in the levels of $F4/80^+$ cells per HPF (UNTX 22.3±10.0 vs. TLS 21.9±9.6 vs. CPOc 22.8±7.3 vs. CPO 35.6±12.0%, $p>0.05$) or $CD206^+$ cells per HPF (UNTX 49.9±10.5 vs. TLS 42.8±8.9 vs. CPOc 44.0±5.5 vs. CPO 47.0±7.2%, $p>0.05$).

<u>While collagen content was not significantly modulated, the lignin composite with CPO exhibited mature collagen architecture over 30 days</u>

Tissue sections were prepared to assess collagen architecture and content over 30 days of healing process from trichrome staining. In rodents, normal tissue has a reticular collagen

pattern, whereas the collagen in scar tissue forms large parallel bundles at approximately right angles to the basement membrane[53]. The CPO lignin composite exhibited more pronounced, bundled mesh network as opposed to relatively straight fibers found in TLS or CPOc lignin composites (**Figure 9a**). Despite qualitative difference of collagen architecture, the quantity of collagen content over 30 days becomes similar to each other (**Figure 9b**). No differences were observed in the overall collagen density between UNTX and TLS- (187.0±23.8 vs. 170.0±26.4 pixels/HPF, $p>0.05$), CPOc- (187.0±23.8 vs. 179.6±21.5 pixels/HPF, $p>0.05$), or CPO- (187.0±23.8 vs. 180.9±29.4 pixels/HPF, $p>0.05$) lignin composite treated wounds. However, reduction of collagen content in a scar has less impact on scarring outcome compared to the structure of matrix deposited in the dermis[54]. Further, wounds treated with the CPO lignin composite left minimal scar as evidenced in photographs taken at 30 days after surgery (**Figure S4**).

DISCUSSION

Application of lignin to wound healing and tissue engineering applications is increasing.

Application of lignin is ever increasing in a number of industrial and biomedical applications, including UV absorption[55], Cu^{2+} chelating in water[56], skin protectants[57], wound dressing with chitosan[58], self-healing smart biomaterials[59], durable and repeatable adhesive[60], antibacterial agent[61,62] with metallic NPs[63], anti-proliferative effect to cancer cells without cytotoxicity[64]. In tissue engineering, lignin composites can be applied to enhance mechanical properties with good protein adsorption capacity and wound compatibility[65], to provide 3D microenvironments of mesenchymal stromal cell culture[58], to confer anti-inflammatory properties by reducing gene expression of iNOS and IL-1β of inflamed mouse Mφ[66], to apply for wound-dressing with biocompatibility and nontoxicity[67], to improve mechanical properties and wound healing capabilities on incision-induced Sprague-Dawley rats[68], to provide nanofibers for the cultures of human dermal fibroblasts (hdFBs)[69], to promote localized and prolonged antioxidant capabilities for wound healing applications[70] and to achieve enhanced mechanical properties and viability of hdFBs for direct ink writing 3D bioprinting[71].

Nevertheless, toxicological studies of lignin have only carried out through simple cytotoxicity testing, which cannot accurately simulate the human body environment. Thus, the biological effects of lignin with animal models should be tested to assess the long-term stability and potential negative effects of lignin and lignin-derived biomaterials. In addition to toxicological studies, another difficulty and key point for the development of lignin-based biomaterials is the heterogeneity of lignin. Although lignin displays good potential for biomedical applications[72], its broad distribution of molecular weight and extremely complex structures represent big hurdles for deep studies, standardization, and scale-up. Thus, lignin chemistry and de/polymerization techniques still need to be continuously developed[73-76].

CaO_2 is widely applied for oxygen generating compounds for tissue regeneration.

The injectable lignin composite can be a unique biomaterial platform to confer antioxidation by TLS and oxygen generation from NPs of CPO without incorporating additional enzymes. Incorporation of CaO_2 into NPs of SLS hydrophilic outer layer and PLGA hydrophobic core[37] allows CaO_2 to be complexed with PLGA. CaO_2 is a white to yellowish powder which has been extensively applied in water treatment, seed disinfection and food processing[77]. When reacted with water at pH lower than 12 (**Figure S5A**), CaO_2 can be decomposed into hydrogen peroxide, hydroxide ions and carbonate, and the generated hydrogen peroxide further decomposes into highly reactive superoxide and hydroxyl radical[78].

The catalase enzyme can decompose the intermediate hydrogen peroxide into water and oxygen. While catalase is an enzyme found in the blood and liver of mammals, this enzyme has to be available *in situ*, not from peroxisome to prevent damages from ROS. This intermediate step eliminates any potential cytotoxic ROS[79]. Without catalase, the cytotoxic byproduct

H_2O_2 may lead to cell damage.[80] Although the actual role of catalase in the oxygen-release process is unclear, decomposition is suggested to take place through the Modified Fenton chemistry – dissociation of H_2O_2 to OH radicals with $Fe^{2+}/^{3+}$[81]. These oxidants react with everything within diffusion limit layer while their half-lives are short. In wound healing, the availability of catalase is limited. Even though the level of expression of catalase mRNA is not changed during wound healing[82], the protein level of catalase is decreased[83]. For example, catalase concentration is reported to be in the range of 50 – 100 U/mL in the oxygen generating gelatin section[84] or 1 mg/mL in the matrix of polycaprolactone (PCL)[85]. In the mixture of CaO_2, catalase and either SLS or TLS, the dissociation of H_2O_2 is predominantly facilitated by catalase and partly by TLS and to less extent by SLS (**Figure S5B**). The native antioxidant properties of SLS or TLS (**Figure S6A**) is maintained at levels of 80% or above of the native antioxidant (*L*-ascorbic acid) up to 50 µg/mL of CaO_2 (**Figure S6B**).

Several cases of CaO_2 incorporation to biomaterials are reported to date. Injectable cryogels are formed with methacrylated hyaluronic acid and CaO_2[86]. Cumulative release of H_2O_2 is up to 468 µmol over 3 h. Microparticles (MP) are formed with the encapsulation of CaO_2 in PCL, then formed composites with GelMA[87]. Over 2 weeks, 2.5 µM of H_2O_2 is released without the formation of MPs while 1.0 µM with the formation of MPs. With 5 to 20 mg/mL of CaO_2, the cumulative release of O_2 is 25% without MP and up to 30% with MP. Some cases include catalase (100 U/mL) and CaO_2 (up to 30 mg/mL)[88,89]. GelMA (50 mg/mL)- CaO_2 (30 mg/mL) with catalase (100 U/mL) releases O_2 up to 5 days[88]. Another type of hydrogel utilizes Ca^{2+} from CaO_2 (up to 10 mg/mL) to crosslink gellan gum (anionic polysaccharide) with catalase[90]. In the matrix of silk/keratin/gelatin, CaO_2 up to 200 mg/mL release O_2 over 2 weeks with additional antibacterial properties for urethral tissue engineering applications[91]. Thiolated gelatin (27 to 63 mg/mL) with CaO_2 (25 to 100 mg/mL) and catalase (2000-5000 U/mg) forms hyperbaric oxygen generating biomaterials.[92] The question is how much CaO_2 is required to efficiently deliver O_2 to tissue microenvironments without causing cytotoxicity. CaO_2 concentrations higher than 10 mg/mL exhibit cytotoxicity to 3T3 FBs[78]. In addition, due to low solubiliuty in water, it is difficult to disperse CaO_2 in aqueous buffers. Further, Ca^{2+} released from these composites influence cell cytotoxicity and bacterial adhesion[93].

To assess the kinetics of O_2, *in situ* oxygen measurement with patch sensors are used[85,92,94]. In the case of measuring concentrations of H_2O_2, Cu(II)-neocuproine spectrophotometric method[95] or free radical analyzer[96] are used. To delineate the difference, the release kinetics of O_2 and H_2O_2 from CaO_2 in water with varying pH and temperature is probed and modeled.[97] The release of H_2O_2 follows pseudo-zero order (PZO) reaction. Once CaO_2 is dissolved in water, Ca^{2+}, O_2^{2-} and H^+ are formed. Of these, $2H^+$ and O_2^{2-} form H_2O_2. With increase of H^+ (decrease of pH), the solubility of CaO_2 is increased. Temperature has minimal to no effect in the kinetics. In contrast, the release of O_2 follows pseudo-first order (PFO) reaction, meaning that the concentration of CaO_2 directly affects the dissociation of CaO_2 to O_2. With the decrease of pH, the release of O_2 is decreased. With the increase of temperature, the release of O_2 increases. From this study of kinetics, H_2O_2 is not necessarily a precursor of O_2.

<u>Locoregional delivery of antioxidation and oxygen generation could be beneficial to accelerate wound healing</u>

WT mice are programmed to heal physiologically with minimal alterations in perfusion and ROS, thus we did not see significantly different results in our measures of wound healing, vessel formation, and inflammation between treatment groups. The translatable benefit of this lignin composite may be more readily apparent in disease states such as diabetic wound healing and/or with infection.

The advanced glycation end products (AGEs) present in diabetic tissue generate ROS leading to FB apoptosis via the NLRP3 (NOD-, LRR- and pyrin domain-containing protein 3) sig-

naling pathway, thus impairing wound repair[98]. Some systemic oral anti-hyperglycemics currently used to treat diabetes mellitus (DM) also have antioxidant and beneficial wound healing effects. Metformin, for example, is a commonly used medication used for glucose control in DM patients which has antioxidant effects and demonstrated benefits on angiogenesis and wound closure in diabetic mice[99]. However, as previously mentioned, pure systemic antioxidants have a poor enteric absorption profile. Locally applied antioxidant hydrogels have been demonstrated to accelerate diabetic wound healing while promoting M2 macrophage differentiation and reducing IL-1β production[100]. Further, topical oxygen delivery to ischemic wounds is shown to accelerate healing and promote granulation tissue formation[101]. The strategy of combining these two wound-beneficial attributes into one local therapy for pathologic wounds has the potential to greatly benefit the wound healing in at-risk patients.

CONCLUSIONS

Lignin has been applied to many different tissue engineering applications. Wound healing applications of lignin has been somewhat limited to doping lignin NPs into a matrix of biomaterials. First, we functionalized lignosulfonate to form lignin composites with TLS. TLS maintained antioxidation capacity in GelMA to attenuate fibrotic responses of hdFBs. Then, we designed NPs of CPO (SLS:PLGA NPs with CPO) to deliver O_2 without cytotoxicity to accelerate wound healing in addition to the antioxidation properties conferred by TLS. The release of O_2 from the CPO lignin composites was around 0.05%/day at least for 7 days. Mechanical properties of lignin composites were not significantly different, but the stiffness set for the *in vivo* applications was amenable to direct M2-like macrophage phenotypes. Swelling and enzymatic degradation of lignin composites *in vitro* were verified before the animal experiments. The area of granulation tissue was modestly increased by the CPO lignin composite while the rate of wound closure was not significantly different by 7 days after surgery. However, the CPO lignin composite increased neovascularization as evidenced by significantly increased blood vessel formation and by the infiltration of αSMA^+ cells to the wound treated with the CPO lignin composite over 7 days. For scar assessment, we sacrificed mice at 30 days after surgery. Although we did observe no difference in the overall collagen density, the collagen architecture treated by the CPO lignin composite exhibited more pronounced, bundled mesh network and left minimal scar. Thus, soft matrix with antioxidation (conferred by TLS) and synergistic oxygen release (NPs of CPO) could be applied to wound healing applications with enhanced tissue granulation, vascularization and maturation of collagen architecture without significant inflammatory responses. Further optimization on the balance between antioxidation and O_2 is in progress, aiming to tackle diabetic wound healing with infection.

AUTHOR CONTRIBUTIONS

JPJ and SB conceived the experiments. JAB, CAE and DS synthesized lignin composites. NTD performed PXIE. SEJ performed swelling, degradation and rheometry of lignin composites. ACG and JCG quantified O_2 and H_2O_2 release from lignin composites. JAB performed fibrosis array. SB, WDS, BWP, TJP and FF did animal surgery and animal data collection. WDS, BWP, TJP, FF, AK, SK and OSJ analyzed the results of animal experiments. JPJ, SB, MK, WDS and BP wrote the manuscript and all authors approved the final manuscript.

ACKNOWLEDGMENTS

The authors acknowledge the support from Gill Plastic Surgery of Houston (SB), Wound Healing Society Foundation FLASH and 3M Award (SB), Clayton Award from Department of Surgery, Texas Children's Hospital (SB), John S. Dunn Foundation Collaborative Research Award (SB), the National Institutes of Health T34GM136452 (SEJ), the National Research Foundation of Korea NRF-2021R1A2C1093999 (DS and MK), the National Science Foundation EPSCoR Track 2 RII, OIA 1632854 (JAB and JPJ) and the National Science Foundation

CAREER DMR 2047018 (JPJ). The authors sincerely acknowledge the technical support received from Ashkan YekrangSafakar and Kidong Park (LSU).

DISCLOSURE
None

REFERENCES

1 Yannas, I. V. & Tzeranis, D. S. Mammals fail to regenerate organs when wound contraction drives scar formation. *NPJ Regen Med* **6**, 39, doi:10.1038/s41536-021-00149-9 (2021).

2 Song, H. G. *et al.* Transient Support from Fibroblasts is Sufficient to Drive Functional Vascularization in Engineered Tissues. *Adv Funct Mater* **30**, doi:10.1002/adfm.202003777 (2020).

3 Kim, S., Lee, H., Chung, M. & Jeon, N. L. Engineering of functional, perfusable 3D microvascular networks on a chip. *Lab Chip* **13**, 1489-1500, doi:10.1039/c3lc41320a (2013).

4 Whisler, J. A., Chen, M. B. & Kamm, R. D. Control of perfusable microvascular network morphology using a multiculture microfluidic system. *Tissue Eng Part C Methods* **20**, 543-552, doi:10.1089/ten.TEC.2013.0370 (2014).

5 Van Linthout, S., Miteva, K. & Tschope, C. Crosstalk between fibroblasts and inflammatory cells. *Cardiovasc Res* **102**, 258-269, doi:10.1093/cvr/cvu062 (2014).

6 Kendall, R. T. & Feghali-Bostwick, C. A. Fibroblasts in fibrosis: novel roles and mediators. *Front Pharmacol* **5**, 123, doi:10.3389/fphar.2014.00123 (2014).

7 Wynn, T. A. & Ramalingam, T. R. Mechanisms of fibrosis: therapeutic translation for fibrotic disease. *Nat Med* **18**, 1028-1040, doi:10.1038/nm.2807 (2012).

8 Holt, D. J., Chamberlain, L. M. & Grainger, D. W. Cell-cell signaling in co-cultures of macrophages and fibroblasts. *Biomaterials* **31**, 9382-9394, doi:10.1016/j.biomaterials.2010.07.101 (2010).

9 Braga, T. T., Agudelo, J. S. & Camara, N. O. Macrophages During the Fibrotic Process: M2 as Friend and Foe. *Front Immunol* **6**, 602, doi:10.3389/fimmu.2015.00602 (2015).

10 Schafer, M. & Werner, S. Oxidative stress in normal and impaired wound repair. *Pharmacol Res* **58**, 165-171, doi:10.1016/j.phrs.2008.06.004 (2008).

11 Dunnill, C. *et al.* Reactive oxygen species (ROS) and wound healing: the functional role of ROS and emerging ROS-modulating technologies for augmentation of the healing process. *Int Wound J* **14**, 89-96, doi:10.1111/iwj.12557 (2017).

12 Nouvong, A., Ambrus, A. M., Zhang, E. R., Hultman, L. & Coller, H. A. Reactive oxygen species and bacterial biofilms in diabetic wound healing. *Physiol Genomics* **48**, 889-896, doi:10.1152/physiolgenomics.00066.2016 (2016).

13 Siwik, D. A., Pagano, P. J. & Colucci, W. S. Oxidative stress regulates collagen synthesis and matrix metalloproteinase activity in cardiac fibroblasts. *Am J Physiol Cell Physiol* **280**, C53-60, doi:10.1152/ajpcell.2001.280.1.C53 (2001).

14 Rendra, E. *et al.* Reactive oxygen species (ROS) in macrophage activation and function in diabetes. *Immunobiology* **224**, 242-253, doi:10.1016/j.imbio.2018.11.010 (2019).

15 Kai, D. *et al.* Sustainable and Antioxidant Lignin–Polyester Copolymers and Nanofibers for Potential Healthcare Applications. *ACS Sustainable Chemistry & Engineering* **5**, 6016-6025, doi:10.1021/acssuschemeng.7b00850 (2017).

16 Hajihashemi, S., Rajabpoor, S. & Djalovic, I. Antioxidant potential in Stevia rebaudiana callus in response to polyethylene glycol, paclobutrazol and gibberellin treatments. *Physiol Mol Biol Plants* **24**, 335-341, doi:10.1007/s12298-017-0498-8 (2018).

17 Javed, R., Ahmed, M., Haq, I. U., Nisa, S. & Zia, M. PVP and PEG doped CuO nanoparticles are more biologically active: Antibacterial, antioxidant, antidiabetic and cytotoxic perspective. *Mater Sci Eng C Mater Biol Appl* **79**, 108-115, doi:10.1016/j.msec.2017.05.006 (2017).

18 Zeng, W. *et al.* Antioxidant treatment enhances human mesenchymal stem cell anti-stress ability and therapeutic efficacy in an acute liver failure model. *Sci Rep* **5**, 11100, doi:10.1038/srep11100 (2015).

19 Choe, G. *et al.* Anti-oxidant activity reinforced reduced graphene oxide/alginate microgels: Mesenchymal stem cell encapsulation and regeneration of infarcted hearts. *Biomaterials* **225**, 119513, doi:10.1016/j.biomaterials.2019.119513 (2019).
20 Sharma, S. K. & Singh, A. P. In vitro antioxidant and free radical scavenging activity of Nardostachys jatamansi DC. *J Acupunct Meridian Stud* **5**, 112-118, doi:10.1016/j.jams.2012.03.002 (2012).
21 Yang, W. *et al.* Polyvinyl alcohol/chitosan hydrogels with enhanced antioxidant and antibacterial properties induced by lignin nanoparticles. *Carbohydr Polym* **181**, 275-284, doi:10.1016/j.carbpol.2017.10.084 (2018).
22 Hosgood, G. Wound healing. The role of platelet-derived growth factor and transforming growth factor beta. *Vet Surg* **22**, 490-495, doi:10.1111/j.1532-950x.1993.tb00426.x (1993).
23 Newsholme, E. A. & Start, C. *Regulation in metabolism*. (1973).
24 Thi, P. L. *et al.* In situ forming and reactive oxygen species-scavenging gelatin hydrogels for enhancing wound healing efficacy. *Acta Biomater* **103**, 142-152, doi:10.1016/j.actbio.2019.12.009 (2020).
25 Li, J. *et al.* N-acetyl cysteine-loaded graphene oxide-collagen hybrid membrane for scarless wound healing. *Theranostics* **9**, 5839-5853, doi:10.7150/thno.34480 (2019).
26 Ninan, N., Forget, A., Shastri, V. P., Voelcker, N. H. & Blencowe, A. Antibacterial and Anti-Inflammatory pH-Responsive Tannic Acid-Carboxylated Agarose Composite Hydrogels for Wound Healing. *ACS Appl Mater Interfaces* **8**, 28511-28521, doi:10.1021/acsami.6b10491 (2016).
27 Wu, H. *et al.* Ceria nanocrystals decorated mesoporous silica nanoparticle based ROS-scavenging tissue adhesive for highly efficient regenerative wound healing. *Biomaterials* **151**, 66-77, doi:10.1016/j.biomaterials.2017.10.018 (2018).
28 Li, Z., Wang, F., Roy, S., Sen, C. K. & Guan, J. Injectable, highly flexible, and thermosensitive hydrogels capable of delivering superoxide dismutase. *Biomacromolecules* **10**, 3306-3316, doi:10.1021/bm900900e (2009).
29 Callahan, L. A. *et al.* ECM production of primary human and bovine chondrocytes in hybrid PEG hydrogels containing type I collagen and hyaluronic acid. *Biomacromolecules* **13**, 1625-1631, doi:10.1021/bm3003336 (2012).
30 Suvarnapathaki, S., Wu, X., Lantigua, D., Nguyen, M. A. & Camci-Unal, G. Breathing life into engineered tissues using oxygen-releasing biomaterials. *NPG Asia Materials* **11**, 65, doi:10.1038/s41427-019-0166-2 (2019).
31 Chevalier, L. & McCann, C. D. Feasibility of calcium peroxide as an oxygen releasing compound in treatment walls. *International Journal of Environment and Waste Management* **2**, 245-256 (2008).
32 Olyaie, E., Banejad, H., Afkhami, A., Rahmani, A. & Khodaveisi, J. Development of a cost-effective technique to remove the arsenic contamination from aqueous solutions by calcium peroxide nanoparticles. *Separation and purification technology* **95**, 10-15 (2012).
33 Waite, A. J., Bonner, J. S. & Autenrieth, R. Kinetics and Stoichiometry of Oxygen Release from Solid Peroxides. *Environmental Engineering Science* **16**, 187-199, doi:10.1089/ees.1999.16.187 (1999).
34 Farris, A. L., Rindone, A. N. & Grayson, W. L. Oxygen Delivering Biomaterials for Tissue Engineering. *J Mater Chem B* **4**, 3422-3432, doi:10.1039/c5tb02635k (2016).
35 Belgodere, J. A. *et al.* Attenuating Fibrotic Markers of Patient-Derived Dermal Fibroblasts by Thiolated Lignin Composites. *ACS Biomater Sci Eng*, doi:10.1021/acsbiomaterials.1c00427 (2021).
36 Belgodere, J. A. *et al.* Modulating Mechanical Properties of Collagen–Lignin Composites. *ACS Applied Bio Materials* **2**, 3562-3572, doi:10.1021/acsabm.9b00444 (2019).

37 Astete, C. E. *et al.* Lignin-Graft-Poly(lactic-co-glycolic) Acid Biopolymers for Polymeric Nanoparticle Synthesis. *ACS Omega* **5**, 9892-9902, doi:10.1021/acsomega.0c00168 (2020).
38 Deoli, N. T. *et al.* Status of the Louisiana accelerator center. *AIP Conference Proceedings* **2160**, 040005, doi:10.1063/1.5127685 (2019).
39 Ryan, C. G. Quantitative trace element imaging using PIXE and the nuclear microprobe. *International Journal of Imaging Systems and Technology* **11**, 219-230 (2000).
40 YekrangSafakar, A., Hamel, K. M., Mehrnezhad, A., Jung, J. P. & Park, K. Development of rolled scaffold for high-density adherent cell culture. *Biomed Microdevices* **22**, 4, doi:10.1007/s10544-019-0459-9 (2019).
41 Deptuła, P. *et al.* Tissue Rheology as a Possible Complementary Procedure to Advance Histological Diagnosis of Colon Cancer. *ACS Biomater Sci Eng* **6**, 5620-5631, doi:10.1021/acsbiomaterials.0c00975 (2020).
42 Demšar, J. *et al.* Orange: data mining toolbox in Python. *the Journal of machine Learning research* **14**, 2349-2353 (2013).
43 Hong, J. H., Kim, D. H., Rhyu, I. J., Kye, Y. C. & Ahn, H. H. A simple morphometric analysis method for dermal microstructure using color thresholding and moments. *Skin Res Technol* **26**, 132-136, doi:10.1111/srt.12776 (2020).
44 Evrosimovska, B., Dimova, C., Kovacevska, I. & Panov, S. Concentration of collagenases (MMP-1, -8, -13) in patients with chronically inflamed dental pulp tissue. *Prilozi* **33**, 191-204 (2012).
45 Manicourt, D. H., Fujimoto, N., Obata, K. & Thonar, E. J. Levels of circulating collagenase, stromelysin-1, and tissue inhibitor of matrix metalloproteinases 1 in patients with rheumatoid arthritis. Relationship to serum levels of antigenic keratan sulfate and systemic parameters of inflammation. *Arthritis Rheum* **38**, 1031-1039, doi:10.1002/art.1780380803 (1995).
46 Khorshidi, S., Karkhaneh, A. & Bonakdar, S. Fabrication of amine-decorated nonspherical microparticles with calcium peroxide cargo for controlled release of oxygen. *J Biomed Mater Res A* **108**, 136-147, doi:10.1002/jbm.a.36799 (2020).
47 Carey, A. V., Carey, R. M. & Gomez, R. A. Expression of alpha-smooth muscle actin in the developing kidney vasculature. *Hypertension* **19**, Ii168-175, doi:10.1161/01.hyp.19.2_suppl.ii168 (1992).
48 Tonino, P. & Abreu, C. Microvessel Density Is Associated with VEGF and α-SMA Expression in Different Regions of Human Gastrointestinal Carcinomas. *Cancers (Basel)* **3**, 3405-3418, doi:10.3390/cancers3033405 (2011).
49 Hamilton, N. B., Attwell, D. & Hall, C. N. Pericyte-mediated regulation of capillary diameter: a component of neurovascular coupling in health and disease. *Front Neuroenergetics* **2**, 5, doi:10.3389/fnene.2010.00005 (2010).
50 Fu, X. *et al.* Specialized fibroblast differentiated states underlie scar formation in the infarcted mouse heart. *J Clin Invest* **128**, 2127-2143, doi:10.1172/jci98215 (2018).
51 Zhuang, Z. *et al.* Control of Matrix Stiffness Using Methacrylate-Gelatin Hydrogels for a Macrophage-Mediated Inflammatory Response. *ACS Biomater Sci Eng* **6**, 3091-3102, doi:10.1021/acsbiomaterials.0c00295 (2020).
52 Kim, S. Y. & Nair, M. G. Macrophages in wound healing: activation and plasticity. *Immunol Cell Biol* **97**, 258-267, doi:10.1111/imcb.12236 (2019).
53 Xue, M. & Jackson, C. J. Extracellular Matrix Reorganization During Wound Healing and Its Impact on Abnormal Scarring. *Advances in wound care* **4**, 119-136, doi:10.1089/wound.2013.0485 (2015).
54 Mascharak, S. *et al.* Preventing Engrailed-1 activation in fibroblasts yields wound regeneration without scarring. *Science* **372**, doi:10.1126/science.aba2374 (2021).

55 Dean, J. C., Navotnaya, P., Parobek, A. P., Clayton, R. M. & Zwier, T. S. Ultraviolet spectroscopy of fundamental lignin subunits: guaiacol, 4-methylguaiacol, syringol, and 4-methylsyringol. *J Chem Phys* **139**, 144313, doi:10.1063/1.4824019 (2013).
56 Todorciuc, T., Bulgariu, L. & Popa, V. I. Adsorption of Cu (II) from aqueous solution on wheat straw lignin: Equilibrium and kinetic studies. *Cell Chem Technol* **49**, 439-447 (2015).
57 Tortora, M. *et al.* Ultrasound driven assembly of lignin into microcapsules for storage and delivery of hydrophobic molecules. *Biomacromolecules* **15**, 1634-1643, doi:10.1021/bm500015j (2014).
58 Ravishankar, K. *et al.* Biocompatible hydrogels of chitosan-alkali lignin for potential wound healing applications. *Mater Sci Eng C Mater Biol Appl* **102**, 447-457, doi:10.1016/j.msec.2019.04.038 (2019).
59 Kai, D. *et al.* Development of lignin supramolecular hydrogels with mechanically responsive and self-healing properties. *ACS Sustainable Chemistry & Engineering* **3**, 2160-2169 (2015).
60 Gan, D. *et al.* Plant-inspired adhesive and tough hydrogel based on Ag-Lignin nanoparticles-triggered dynamic redox catechol chemistry. *Nat Commun* **10**, 1487, doi:10.1038/s41467-019-09351-2 (2019).
61 Gabov, K., Oja, T., Deguchi, T., Fallarero, A. & Fardim, P. Preparation, characterization and antimicrobial application of hybrid cellulose-lignin beads. *Cellulose* **24**, 641-658 (2017).
62 Gregorova, A., Redik, S., Sedlarik, V. & Stelzer, F. in *Proceedings, 3rd Int. Conf.* 184-189.
63 Li, P., Lv, W. & Ai, S. Green and gentle synthesis of Cu2O nanoparticles using lignin as reducing and capping reagent with antibacterial properties. *Journal of Experimental Nanoscience* **11**, 18-27 (2016).
64 Figueiredo, P. *et al.* In vitro evaluation of biodegradable lignin-based nanoparticles for drug delivery and enhanced antiproliferation effect in cancer cells. *Biomaterials* **121**, 97-108, doi:10.1016/j.biomaterials.2016.12.034 (2017).
65 Zhang, Y. *et al.* Novel lignin-chitosan-PVA composite hydrogel for wound dressing. *Mater Sci Eng C Mater Biol Appl* **104**, 110002, doi:10.1016/j.msec.2019.110002 (2019).
66 Mahata, D. *et al.* Lignin-graft-Polyoxazoline Conjugated Triazole a Novel Anti-Infective Ointment to Control Persistent Inflammation. *Sci Rep* **7**, 46412, doi:10.1038/srep46412 (2017).
67 Xu, J. *et al.* Lignin-Incorporated Nanogel Serving As an Antioxidant Biomaterial for Wound Healing. *ACS Appl Bio Mater* **4**, 3-13, doi:10.1021/acsabm.0c00858 (2021).
68 Jaiswal, L., Shankar, S., Rhim, J. W. & Hahm, D. H. Lignin-mediated green synthesis of AgNPs in carrageenan matrix for wound dressing applications. *Int J Biol Macromol* **159**, 859-869, doi:10.1016/j.ijbiomac.2020.05.145 (2020).
69 Kai, D., Jiang, S., Low, Z. W. & Loh, X. J. Engineering highly stretchable lignin-based electrospun nanofibers for potential biomedical applications. *J Mater Chem B* **3**, 6194-6204, doi:10.1039/c5tb00765h (2015).
70 Domínguez-Robles, J. *et al.* Antioxidant PLA Composites Containing Lignin for 3D Printing Applications: A Potential Material for Healthcare Applications. *Pharmaceutics* **11**, doi:10.3390/pharmaceutics11040165 (2019).
71 Oveissi, F., Naficy, S., Le, T. Y. L., Fletcher, D. F. & Dehghani, F. Tough and Processable Hydrogels Based on Lignin and Hydrophilic Polyurethane. *ACS Appl Bio Mater* **1**, 2073-2081, doi:10.1021/acsabm.8b00546 (2018).
72 Liu, R. *et al.* Lignin-Based Micro- and Nanomaterials and their Composites in Biomedical Applications. *ChemSusChem* **13**, 4266-4283, doi:10.1002/cssc.202000783 (2020).

73 Moradipour, M. *et al.* Interaction of lignin-derived dimer and eugenol-functionalized silica nanoparticles with supported lipid bilayers. *Colloids Surf B Biointerfaces* **191**, 111028, doi:10.1016/j.colsurfb.2020.111028 (2020).
74 Tong, X. *et al.* Experimental and Molecular Dynamics Simulation Study of the Effects of Lignin Dimers on the Gel-to-Fluid Phase Transition in DPPC Bilayers. *J Phys Chem B* **123**, 8247-8260, doi:10.1021/acs.jpcb.9b05525 (2019).
75 Moradipour, M. *et al.* Interaction of lignin dimers with model cell membranes: A quartz crystal microbalance and molecular dynamics simulation study. *Biointerphases* **16**, 041003, doi:10.1116/6.0001029 (2021).
76 Lee, J. G. *et al.* Lignin–Zein Composite: Synthesis, Three-Dimensional Printing, and Microbial Degradation. *ACS Sustainable Chemistry & Engineering* **9**, 1781-1789, doi:10.1021/acssuschemeng.0c07915 (2021).
77 Zhai, J. & Jiang, C. H. in *Advanced Materials Research.* 648-653 (Trans Tech Publ).
78 Novotortsev, V. M. *et al.* Examination of the disinfecting properties of calcium peroxide and its suitability for improving hydrodynamic characteristics of surface water bodies. *Russian Journal of Applied Chemistry* **85**, 726-730, doi:10.1134/S1070427212050072 (2012).
79 Camci-Unal, G., Annabi, N., Dokmeci, M. R., Liao, R. & Khademhosseini, A. Hydrogels for cardiac tissue engineering. *NPG Asia Materials* **6**, e99-e99, doi:10.1038/am.2014.19 (2014).
80 Ashammakhi, N. *et al.* Advances in Controlled Oxygen Generating Biomaterials for Tissue Engineering and Regenerative Therapy. *Biomacromolecules* **21**, 56-72, doi:10.1021/acs.biomac.9b00546 (2020).
81 Lewis, M. C., Macarthur, B. D., Malda, J., Pettet, G. & Please, C. P. Heterogeneous proliferation within engineered cartilaginous tissue: the role of oxygen tension. *Biotechnol Bioeng* **91**, 607-615, doi:10.1002/bit.20508 (2005).
82 Steiling, H., Munz, B., Werner, S. & Brauchle, M. Different types of ROS-scavenging enzymes are expressed during cutaneous wound repair. *Exp Cell Res* **247**, 484-494, doi:10.1006/excr.1998.4366 (1999).
83 Iuchi, Y. *et al.* Spontaneous skin damage and delayed wound healing in SOD1-deficient mice. *Mol Cell Biochem* **341**, 181-194, doi:10.1007/s11010-010-0449-y (2010).
84 Kang, J. I. & Park, K. M. Advances in gelatin-based hydrogels for wound management. *J Mater Chem B* **9**, 1503-1520, doi:10.1039/d0tb02582h (2021).
85 Suvarnapathaki, S., Nguyen, M. A., Goulopoulos, A. A., Lantigua, D. & Camci-Unal, G. Engineering calcium peroxide based oxygen generating scaffolds for tissue survival. *Biomater Sci* **9**, 2519-2532, doi:10.1039/d0bm02048f (2021).
86 Joshi Navare, K. *et al.* Needle-injectable microcomposite cryogel scaffolds with antimicrobial properties. *Scientific Reports* **10**, 18370, doi:10.1038/s41598-020-75196-1 (2020).
87 Hassan, S. *et al.* Survival and Proliferation under Severely Hypoxic Microenvironments Using Cell-Laden Oxygenating Hydrogels. *J Funct Biomater* **12**, doi:10.3390/jfb12020030 (2021).
88 Alemdar, N. *et al.* Oxygen-Generating Photo-Cross-Linkable Hydrogels Support Cardiac Progenitor Cell Survival by Reducing Hypoxia-Induced Necrosis. *ACS Biomaterials Science & Engineering* **3**, 1964-1971, doi:10.1021/acsbiomaterials.6b00109 (2017).
89 Erdem, A. *et al.* 3D Bioprinting of Oxygenated Cell-Laden Gelatin Methacryloyl Constructs. *Advanced Healthcare Materials* **9**, 1901794, doi:doi:10.1002/adhm.201901794 (2020).
90 Newland, B., Baeger, M., Eigel, D., Newland, H. & Werner, C. Oxygen-Producing Gellan Gum Hydrogels for Dual Delivery of Either Oxygen or Peroxide with Doxorubicin. *ACS Biomater Sci Eng* **3**, 787-792, doi:10.1021/acsbiomaterials.7b00078 (2017).

91 Lv, X. *et al.* Structural and functional evaluation of oxygenating keratin/silk fibroin scaffold and initial assessment of their potential for urethral tissue engineering. *Biomaterials* **84**, 99-110, doi:10.1016/j.biomaterials.2016.01.032 (2016).
92 Park, S. & Park, K. M. Hyperbaric oxygen-generating hydrogels. *Biomaterials* **182**, 234-244, doi:10.1016/j.biomaterials.2018.08.032 (2018).
93 Thi, P. L. *et al.* Calcium peroxide-mediated in situ formation of multifunctional hydrogels with enhanced mesenchymal stem cell behaviors and antibacterial properties. *Journal of Materials Chemistry B* **8**, 11033-11043, doi:10.1039/D0TB02119A (2020).
94 Park, K. M., Blatchley, M. R. & Gerecht, S. The design of dextran-based hypoxia-inducible hydrogels via in situ oxygen-consuming reaction. *Macromol Rapid Commun* **35**, 1968-1975, doi:10.1002/marc.201400369 (2014).
95 Lee, Y. *et al.* In Situ Forming and H(2)O(2)-Releasing Hydrogels for Treatment of Drug-Resistant Bacterial Infections. *ACS Appl Mater Interfaces* **9**, 16890-16899, doi:10.1021/acsami.7b03870 (2017).
96 Heble, A. Y., Santelli, J., Armstrong, A. M., Mattrey, R. F. & Lux, J. Catalase-Loaded Silica Nanoparticles Formulated via Direct Surface Modification as Potential Oxygen Generators for Hypoxia Relief. *ACS Appl Mater Interfaces* **13**, 5945-5954, doi:10.1021/acsami.0c19633 (2021).
97 Wang, H. *et al.* Properties of calcium peroxide for release of hydrogen peroxide and oxygen: A kinetics study. *Chemical Engineering Journal* **303**, 450-457, doi:doi:10.1016/j.cej.2016.05.123 (2016).
98 Dai, J., Chen, H. & Chai, Y. Advanced Glycation End Products (AGEs) Induce Apoptosis of Fibroblasts by Activation of NLRP3 Inflammasome via Reactive Oxygen Species (ROS) Signaling Pathway. *Med Sci Monit* **25**, 7499-7508, doi:10.12659/msm.915806 (2019).
99 Han, X. *et al.* Metformin accelerates wound healing in type 2 diabetic db/db mice. *Mol Med Rep* **16**, 8691-8698, doi:10.3892/mmr.2017.7707 (2017).
100 Zhao, H. *et al.* ROS-scavenging hydrogel to promote healing of bacteria infected diabetic wounds. *Biomaterials* **258**, 120286, doi:10.1016/j.biomaterials.2020.120286 (2020).
101 Rao, C. *et al.* Effects of topical oxygen therapy on ischemic wound healing. *J Phys Ther Sci* **28**, 118-123, doi:10.1589/jpts.28.118 (2016).

FIGURES

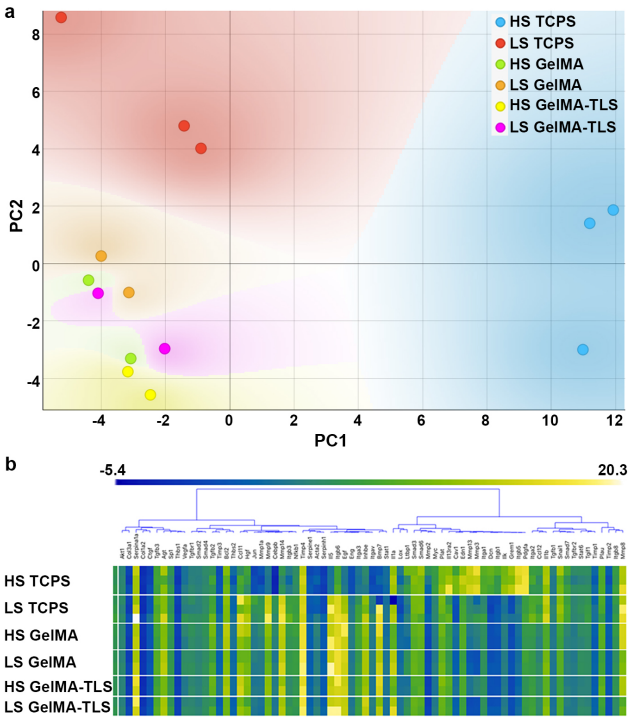

Figure 1. Fibrosis array of human dermal fibroblasts (hdFBs). (a) PCA of 84 fibrosis-related genes from high scar (HS) and low scar (LS) hdFBs cultured on three different substrates (TCPS, GelMA and GelMA-TLS). (b) HC of 84 fibrosis-related gene. LS exhibits a proliferative phenotype. Both GelMA or GelMA-TLS composites modulates the profiles of the fibrosis-related genes.

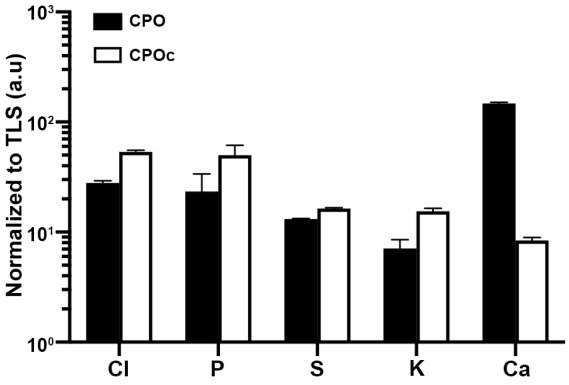

Figure 2. Elemental analysis of NPs of CPO and CPOc by microPXIE. The concentration (arbitrary units, a.u.) of Cl, P, S, K and Ca in NPs of CPO and CPOc (NPs without CPO) normalized to NPs of TLS. The bars represent counting uncertainties (1σ) in a single measurement analyzed by GeoPIXE software; mean±SEM.

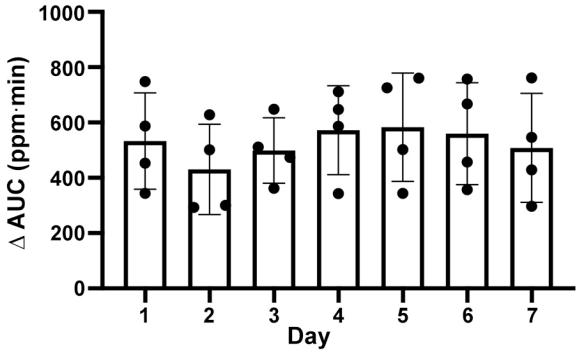

Figure 3. Quantification of O_2 from lignin composites with NPs of CPO. Oxygen released from lignin composites with NPs of CPO was measured using a planar O_2 sensor attached to the bottom of a well in a 96-well plate. Area under curve (AUC) was calculated and the differential between the lignin composites with NPs of CPO and that with CPOc (4 mg/mL) over 1440 min was reported. One-way ANOVA with Tukey's *post hoc* test, no significant difference to each other; mean±SD, n=4.

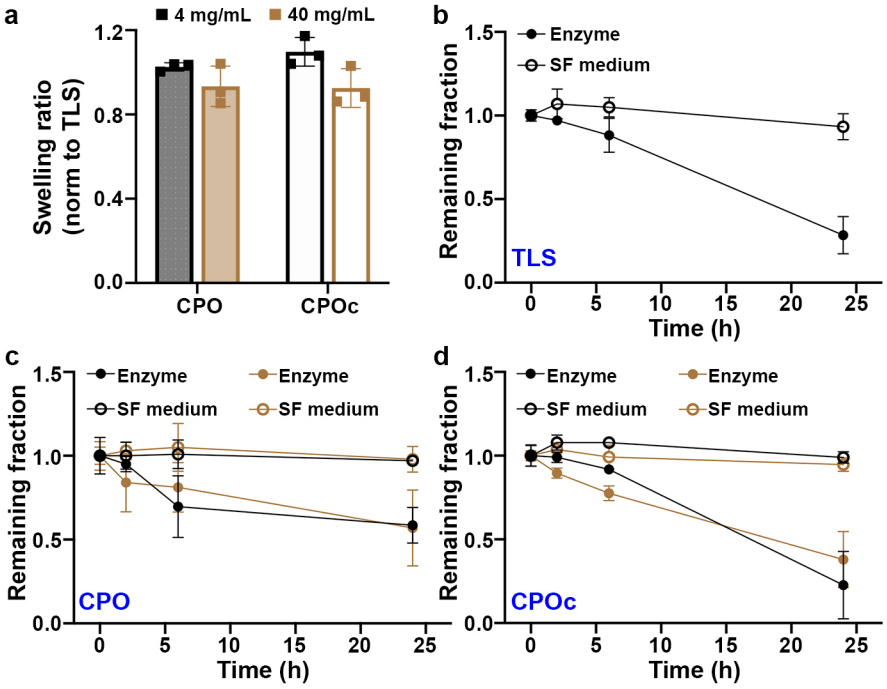

Figure 4. Swelling ratios and degradation of CPO and CPOc lignin composites. (a) Swelling ratios normalized to TLS lignin composites. No statistical difference between CPO and CPOc lignin composites at the same concentration and between two different concentrations at each composite type. Student's *t*-test showed no statistically significant difference; mean±SD, n=3. Degradation of lignin composites, TLS (b), CPO (c) and CPOc (d), in the solution of 0.5 U/mL collagenase (enzyme) or serum-free medium (SF medium). In (c) and (d), black and brown symbols represent the concentrations of NPs (wither CPO or CPOc) at 4 and 40 mg/mL, respectively; mean±SD, n=3.

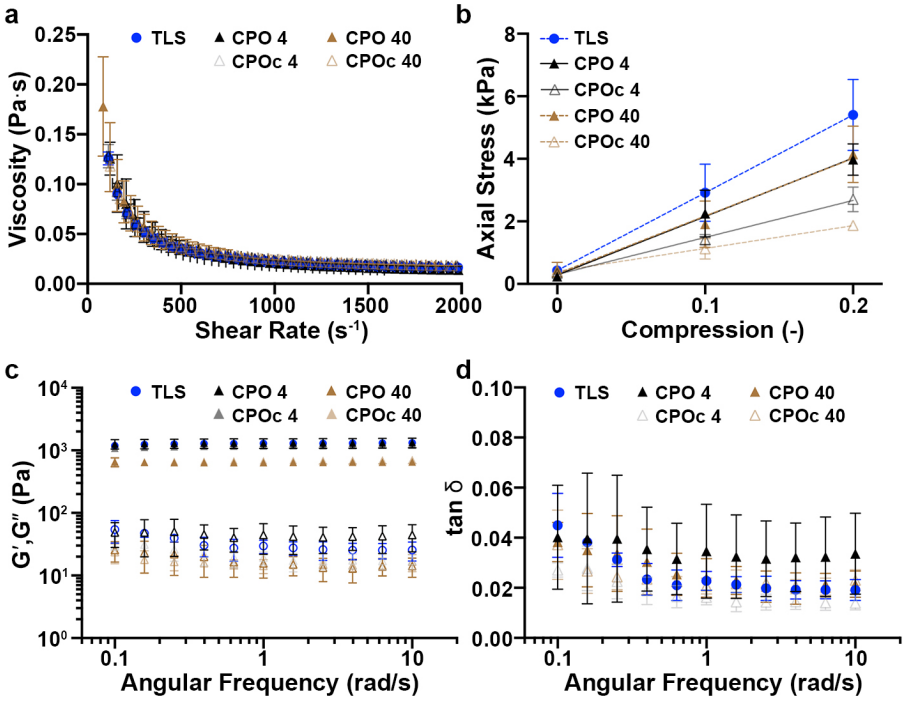

Figure 5. Oscillating rheometry of lignin composites. (a) Viscosity of each precursor before photo-crosslinking. (b) Axial stresses are plotted against compression varying from 0 to 20%. (c) Frequency sweeping of lignin composites. Solid and open symbols represent G′ (storage modulus) and G″ (loss modulus), respectively. (d) Loss tangent (δ) of lignin composites from 0.1 to 10 rad/s. mean±SD, n=3 for all samples.

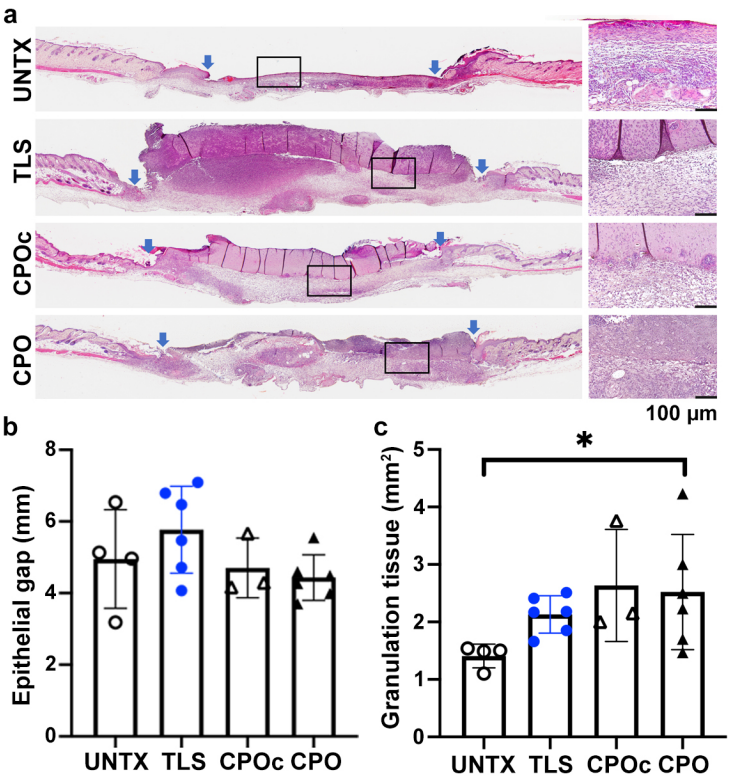

Figure 6. Morphometric analysis of wounds treated with lignin composites at 7 days after surgery. Wounds in WT C57BL/6N mice were treated with lignin composites (a) to measure epithelial gap (b) and granulation tissue area (c). In (a), boxed areas are provided in inset images at higher magnification of hematoxylin (blue, nuclei) and eosin (red, ECM and cytoplasm) staining. UNTX, untreated; TLS, GelMA-TLS; CPOc, GelMA-TLS-CPOc (CPO control); CPO, GelMA-TLS-CPO. Scale bar, 100 µm. One-way ANOVA with Kruskal-Wallis test followed by Dunn's multiple comparison test. *$p<0.05$. $3 \leq n \leq 6$, mean±SD.

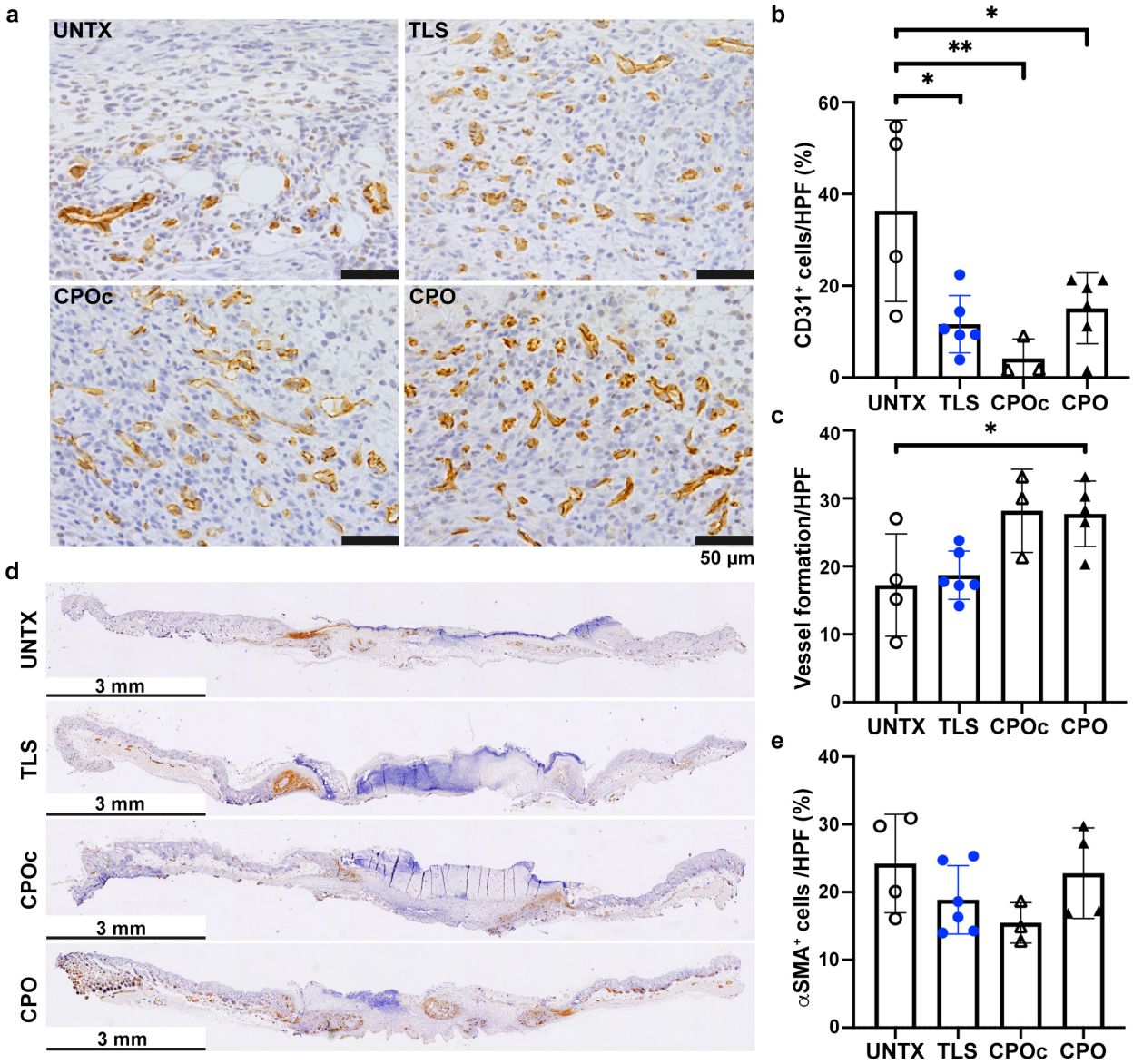

Figure 7. Assessment of vascularization in the wounds treated with lignin composites at 7 days after surgery. Wounds in WT C57BL/6N mice were treated with lignin composites to assess the extent of vascularization with immunostaining (CD31, brown) and hematoxylin counterstaining (blue, nuclei). $CD31^+$ cells (b) and vessel formation (c) per HPF were quantified. The infiltration of αSMA^+ cells to wounds was visualized (d) and quantified per HPF (e). UNTX, untreated; TLS, GelMA-TLS; CPOc, GelMA-TLS-CPOc (CPO control); CPO, GelMA-TLS-CPO. Scale bars, 50 μm in (a) and 3 mm in (d), respectively. One-way ANOVA with Tukey's *post hoc* tests, $^{**}p<0.01$ and $^{*}p<0.05$. $3 \leq n \leq 6$, mean±SD.

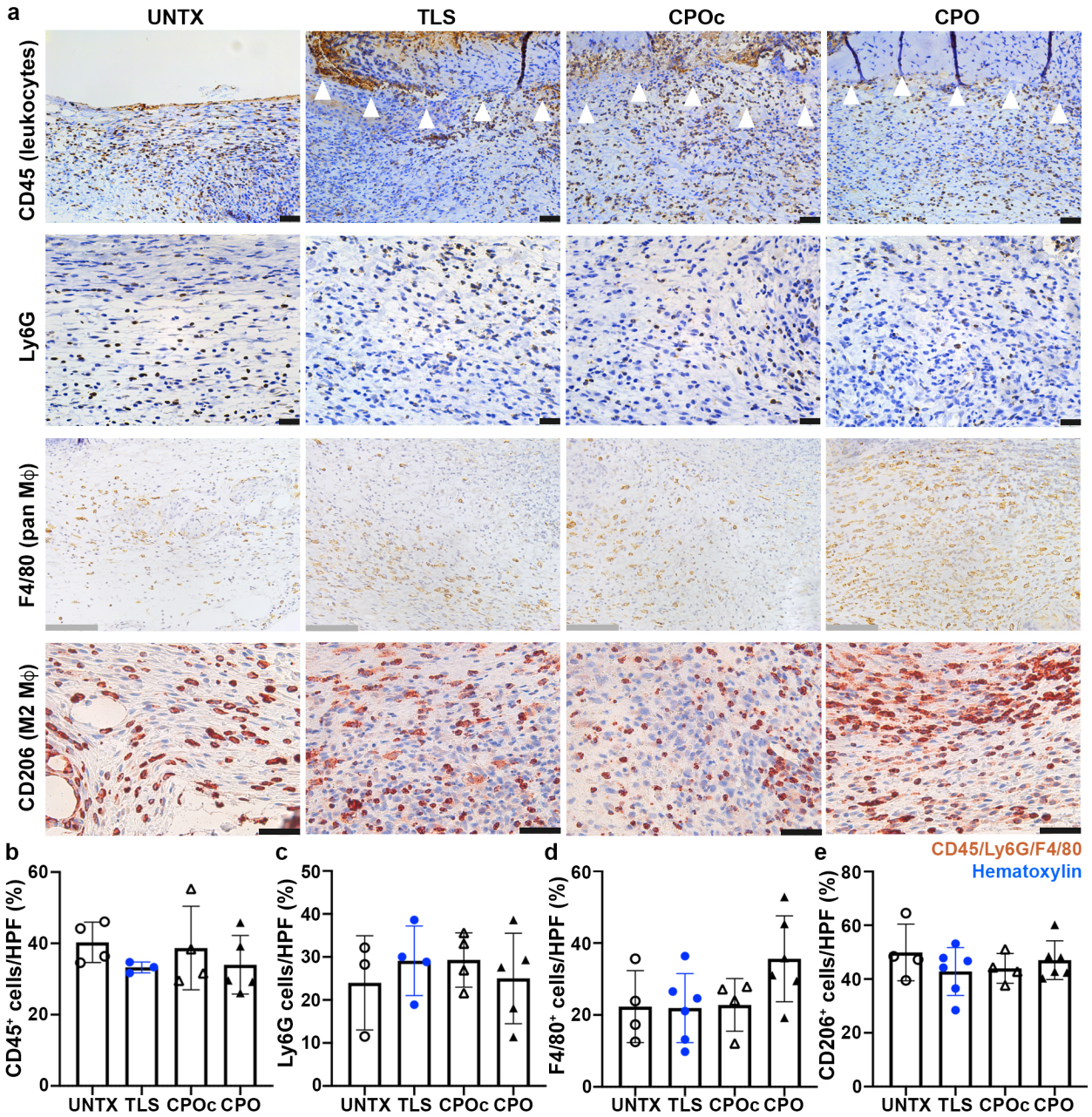

Figure 8. Assessment of inflammatory responses from the wounds treated with lignin composites at 7 days after surgery. Wounds in WT C57BL/6N mice were treated with lignin composites to assess the extent of inflammatory responses (a) with immunohistochemical staining and hematoxylin counterstaining (blue, nuclei). $CD45^+$ leukocytes (b), $Ly6G^+$ monocytes, granulocytes, and neutrophils (c), $F4/80^+$ pan Mφ (d) and CD206 M2 Mφ (e) per HPF were quantified. UNTX, untreated; TLS, GelMA-TLS; CPOc, GelMA-TLS-CPOc (CPO control); CPO, GelMA-TLS-CPO. In (a), black scale bars, 50 μm and grey scale bars, 125 μm, respectively. $3 \leq n \leq 6$, mean±SD.

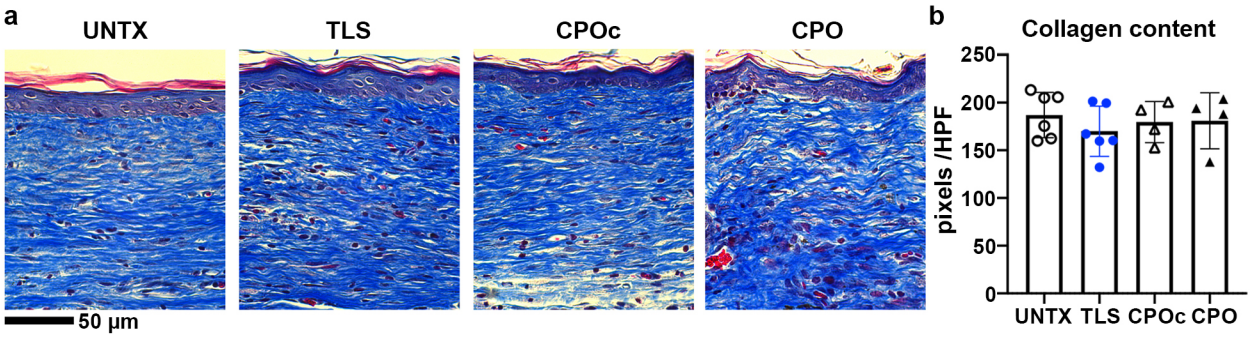

Figure 9. Scar assessment in the wounds treated with lignin composites at 30 days after surgery. Wounds in WT C57BL/6N mice were treated with lignin composites to assess the collagen content with trichrome (blue, collagen) (a). Collagen content was quantified per HPF using color moment thresholding in ImageJ (b). UNTX, untreated; TLS, GelMA-TLS; CPOc, GelMA-TLS-CPOc (CPO control); CPO, GelMA-TLS-CPO. Scale bar, 50 µm. 3≤n≤6, mean±SD.